

## Asymmetric Cherenkov emission in a topological plasmonic waveguide

Filipa R. Prudêncio<sup>1,2,\*</sup> and Mário G. Silveirinha<sup>1</sup>

<sup>1</sup>University of Lisbon – Instituto Superior Técnico and Instituto de Telecomunicações, Avenida Rovisco Pais 1, 1049-001 Lisboa, Portugal

<sup>2</sup>Instituto Universitário de Lisboa (ISCTE-IUL), 1649-026 Lisboa, Portugal



(Received 20 June 2018; published 20 September 2018)

Here, we investigate the Cherenkov emission by an array of moving electric charges in the vicinity of a topologically nontrivial gyrotropic material. It is shown that the nonreciprocal material response may result in a robustly asymmetric Cherenkov emission, such that the spectrum of the emitted radiation and the stopping power depend strongly on the sign of the particle velocity. It is demonstrated that the main emission channels are determined by the unidirectional edge states supported by the topological material. We consider as examples both magnetized plasmas and Weyl semimetals. The latter may exhibit a spontaneous nonreciprocal response without a biasing magnetic field.

DOI: [10.1103/PhysRevB.98.115136](https://doi.org/10.1103/PhysRevB.98.115136)

### I. INTRODUCTION

The use of topological methods in photonics opened up a myriad of novel photonic platforms with fascinating properties [1–8]. In particular, Chern topological insulators are nonreciprocal structures (e.g., photonic crystals) characterized by a (nontrivial) topological invariant called the Chern number [1,2]. The topological invariant depends on the material band structure [1] and determines the net number of topologically protected unidirectional edge states supported by an interface of the material and another “mirror” with a trivial topology and a common band gap [1,2]. The edge states are protected against backscattering and this unique and singular property has inspired the development of many novel photonic platforms insensitive to imperfections and to back-reflections [1–8]. Some reciprocal material platforms with a bianisotropic response also have a topological classification [9–12]. Moreover, the ideas of topological photonics can be extended to a continuum with no intrinsic periodicity [6,7], and gyrotropic media are generically topologically nontrivial. Recently, it was shown that the photonic Chern number has a precise physical meaning: it can be understood as the *quantum* of the thermally generated light-angular momentum in a closed cavity filled with the photonic insulator [13].

Typically, nontrivial topological materials require some external biasing to break the time-reversal symmetry [1,2], e.g., a magnetic bias. Remarkably, it was recently predicted that a new class of electronic topological materials called Weyl semimetals [14–17] may exhibit a spontaneous nonreciprocal response without any external magnetic field due to magnetic order. Weyl semimetals have unusual properties, for example, the electrons in a fully three-dimensional solid are described by the massless relativistic Dirac equation [14,15].

The Cherenkov effect [18–20] occurs when a charged particle moves inside or nearby a transparent medium with a velocity  $v$  larger than the phase velocity of light in the medium. In recent years, there has been a renewed interest

in this fundamental effect, largely motivated by the discovery of photonic crystals and metamaterials and by the fact that such structures can lead to exotic forms of Cherenkov radiation [21–23]. In particular, Veselago theoretically predicted in 1967 that a moving particle in a left-handed material produces both forward and reversed Cherenkov radiation [21]. More recently, the light emission by swift electrons and by more general moving sources was investigated in plasmonic platforms, in 2D materials such as graphene, and in metamaterials with a plasmonic-type hyperbolic response [24–33]. The Cherenkov radiation has relevant applications in free-electron lasers, biomedicine, particle detection, and nanoscale light sources [34].

In this article, we investigate the impact of a nontrivial material topology in the context of the Cherenkov radiation. We consider a beam of electric charges moving in a vacuum in the vicinity of (i) a magnetized plasma (e.g., a magnetized semiconductor) (ii) a Weyl semimetal characterized by a spontaneous nonreciprocal response. We find that the unidirectional plasmon edge waves are the main radiation channels and lead to strongly asymmetric Cherenkov radiation with spectrum depending on the sign of the electrons velocity. Moreover, the studied platforms may behave as “Cherenkov diodes” such that the amount of emitted radiation depends on the sign of the velocity, which may be useful in detectors where it is important to discriminate the sign of the particle velocity.

The article is organized as follows. In Sec. II, we present the theoretical formalism for a “pencil beam” of charges. In Sec. III, we study the Cherenkov emission by charged particles moving in the vicinity of either a magnetized plasma or a Weyl semimetal. In Sec. IV, some of our findings are generalized to the case of a “pointlike” beam and the stopping power is analytically calculated. Finally, in Sec. V, the main conclusions are drawn.

### II. THEORY FOR A PENCIL OF MOVING CHARGES

For simplicity, in a first stage, we suppose that the relevant beam of charges is shaped in the form of a “pencil”, i.e., it corresponds to a linear array of charges moving in a vacuum

\*Corresponding author: [filipa.prudencio@lx.it.pt](mailto:filipa.prudencio@lx.it.pt)

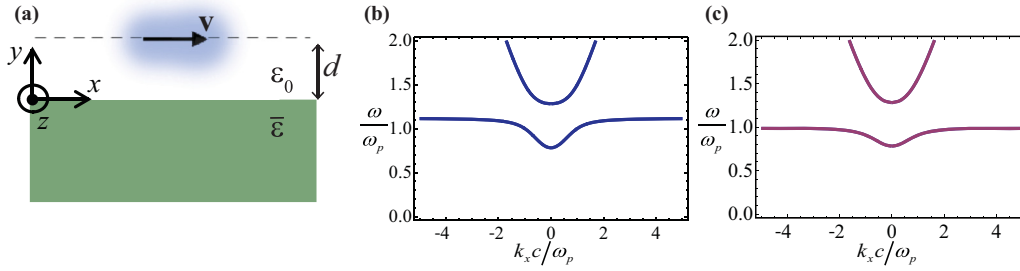


FIG. 1. (a) A linear array of charged particles moves with a constant velocity  $v$  at a distance  $d$  from either a (i) magnetized plasma (biased along the  $z$  direction) or a Weyl semimetal. (b) Band diagram of the natural plane-wave modes for a bulk magnetized plasma. (c) Band diagram of the natural plane-wave modes for a bulk Weyl semimetal.

near the topological material. The charges move along the  $x$  direction with a constant velocity  $v$  at a distance  $d$  from a gyrotropic material occupying the negative  $y$  half-space [Fig. 1(a)]. The current density describing this pencil beam is  $\mathbf{j}_e(x, y, t) = -en_z v \delta(y - y_0) \delta(x - vt) \hat{\mathbf{x}}$ , where  $-e$  is the electron charge,  $n_z$  is the number of charges per unit of length along the  $z$  direction, and  $y_0 = d$ . The outlined problem is effectively two-dimensional which eases the analytical developments. In Sec. IV, we generalize some of our results to the fully 3D scenario.

The Cherenkov radiation emitted by the linear array of charges is determined by the Maxwell equations,  $\partial \mathbf{B} / \partial t + \nabla \times \mathbf{E} = 0$  and  $\nabla \times \mathbf{H} - \partial \mathbf{D} / \partial t = \mathbf{j}_e$ . For a pencil beam, the fields are of the form  $H = H_z(x, y, t) \hat{\mathbf{z}}$  and  $\mathbf{E} = E_x(x, y, t) \hat{\mathbf{x}} + E_y(x, y, t) \hat{\mathbf{y}}$ . It is convenient to work in the frequency (Fourier transform) domain. The Fourier transform of the electric current density [ $\mathbf{j}_e(x, y, \omega) = \int_{-\infty}^{+\infty} \mathbf{j}_e(x, y, t) e^{+i\omega t} dt$ ] is  $\mathbf{j}_e(x, y, \omega) = -en_z \text{sgn}(v) \delta(y - y_0) e^{ik_x x} \hat{\mathbf{x}}$  where  $k_x = \omega/v$  and  $y_0 = d$ .

The electric gyrotropic material half-space is characterized by the generic (relative) permittivity tensor  $\bar{\epsilon} = \epsilon_t \mathbf{1}_t + \epsilon_a \hat{\mathbf{z}} \otimes \hat{\mathbf{z}} + i\epsilon_g \hat{\mathbf{z}} \times \mathbf{1}$  with  $\mathbf{1}_t = \mathbf{1} - \hat{\mathbf{z}} \otimes \hat{\mathbf{z}}$ . Then, the magnetic field in the frequency domain is of the form

$$H_z(x, y, \omega) = \begin{cases} A e^{-\gamma_0 y} e^{ik_x x}, & y > y_0 \\ B(e^{+\gamma_0 y} + R e^{-\gamma_0 y}) e^{ik_x x}, & 0 < y < y_0, \\ B T e^{\gamma_g y} e^{ik_x x}, & y < 0 \end{cases} \quad (1)$$

$$H_z(x, y, \omega) = \frac{1}{2} n_z e \text{sgn}(v) h_z(x, y, \omega), \quad h_z(x, y, \omega) = \begin{cases} [\text{sgn}(-y + y_0) e^{-\gamma_0 |y - y_0|} + R e^{-\gamma_0 (y + y_0)}] e^{ik_x x}, & y > 0 \\ e^{-\gamma_0 y_0} T e^{\gamma_g y} e^{ik_x x}, & y < 0 \end{cases} \quad (4)$$

Applying the inverse Fourier transform, one finds the time-domain magnetic field:

$$H_z(x, y, t) = \frac{1}{2} n_z e \text{sgn}(v) \omega_p h_z(x, y, t), \quad (5)$$

$$h_z(x, y, t) = \frac{1}{2\pi} \int_{-\infty}^{+\infty} h_z(x, y, \omega) e^{-i\omega t} \frac{d\omega}{\omega_p}.$$

The normalization parameter  $\omega_p$  (with unities of frequency) was introduced so that the function  $h_z(x, y, t)$  is dimension-

less. In the numerical examples,  $\omega_p$  will correspond to the plasma frequency of the relevant material. It is simple to prove that the dependence in time of the magnetic field is of the form  $H_z(x, y, t) = H_z(x - vt, y, t = 0)$ . Hence the emitted fields are characterized by a single snapshot in time. The amount of energy extracted from the moving charges is the so-called ‘‘stopping power.’’ Since the velocity of the charges is assumed time-independent, it may be written as  $P_{\text{ext}} = -\int \mathbf{E}_{\text{loc}} \cdot \mathbf{j}_e d^3 \mathbf{r}$ , where  $\mathbf{E}_{\text{loc}}$  represents the local electric field that acts on the charges and  $\mathbf{j}_e(x, y, t)$  is the

$$A = -en_z \text{sgn}(v) \frac{1}{2} (e^{+\gamma_0 y_0} - e^{-\gamma_0 y_0} R),$$

$$B = en_z \text{sgn}(v) \frac{e^{-\gamma_0 y_0}}{2}. \quad (2)$$

Evidently,  $R$  and  $T$  can be identified as the reflection and transmission coefficients for plane wave incidence at a single interface between the vacuum and the gyrotropic material. Using mode matching one easily finds that [7]

$$R = \frac{\frac{\gamma_0}{\epsilon_0} - \left( \frac{\gamma_g}{\epsilon_{ef}} + ik_x \frac{\epsilon_{12}}{\epsilon_{11} + \epsilon_{12}^2} \right)}{\frac{\gamma_0}{\epsilon_0} + \left( \frac{\gamma_g}{\epsilon_{ef}} + ik_x \frac{\epsilon_{12}}{\epsilon_{11} + \epsilon_{12}^2} \right)}, \quad T = 1 + R. \quad (3)$$

From Eq. (2), the frequency domain magnetic field may be written in a more compact manner as

electric current density in the time domain. It can be written explicitly as

$$\frac{P_{\text{ext}}}{L_z} = \frac{P_0}{y_0} \int_{-\infty}^{+\infty} G(\omega) \frac{d\omega}{\omega_p}, \quad (6)$$

where  $P_0 = \frac{n_z^2 e^2}{4\pi \epsilon_0} c$  is a normalization factor (with units of power),  $L_z$  represents the width of the current pencil along the  $z$  direction and

$$G(\omega) = \text{Re} \left\{ \frac{|v|}{c} \gamma_0 y_0 \frac{\omega_p}{i\omega} R e^{-2\gamma_0 y_0} \right\} \quad (7)$$

is the (bilateral) normalized power spectral density that determines the spectrum of the emitted radiation.

### III. CHERENKOV EMISSION IN THE VICINITY OF A GYROTROPIC HALF-SPACE

#### A. Magnetized plasma

For the particular case of a magnetized electron gas (e.g., a magnetized semiconductor [35]), the components of the permittivity tensor are [36]

$$\begin{aligned} \epsilon_t &= 1 - \frac{\omega_p^2 (i\Gamma + \omega)}{\omega (i\Gamma + \omega)^2 - \omega \omega_0^2}, \\ \epsilon_a &= 1 - \frac{1}{\omega} \frac{\omega_p^2}{(i\Gamma + \omega)}, \\ \epsilon_g &= \frac{1}{\omega} \frac{\omega_0 \omega_p^2}{\omega_0^2 - (i\Gamma + \omega)^2}, \end{aligned} \quad (8)$$

where  $\omega_p$  is the plasma frequency,  $\omega_0 = -q B_0 / m^*$  is the cyclotron frequency ( $q = -e$  is the negative charge of the electrons and  $m^*$  is the effective mass),  $\mathbf{B}_0 = B_0 \hat{\mathbf{z}}$  is the biasing magnetic field, and  $\Gamma$  is the collision frequency. Note that the theory of Sec. II neglects the influence of the magnetic field bias on the trajectory of the pencil beam. This is acceptable if the interaction of the moving charges with the gyrotropic material is confined to a limited spatial region, as in the case of a real experiment. In Appendix A, it is shown that the deflection due to the magnetic field may be negligible for heavy charged particles (e.g., protons) even for fairly large values of  $B_0$ .

The band diagram of an unbounded (bulk) gyrotropic medium ( $\omega = \omega_k^{\text{bulk}}$ ) is found from the solution of  $k^2 = \epsilon_{ef} \omega^2 / c^2$  (for propagation in the  $xoy$  plane, perpendicular to the bias field), and is plotted in Fig. 1(b) for the parameters  $\omega_0 = 0.5\omega_p$  and  $\Gamma = 0^+$ . As seen, it exhibits a spectral symmetry such that  $\omega_{k_x}^{\text{bulk}} = \omega_{-k_x}^{\text{bulk}}$ .

The surface plasmons [see Eq. (9)] supported by the interface between the vacuum and the topological material half-space are determined by the dispersion equation [6,7,37–39],

$$\frac{\gamma_0}{\epsilon_0} + \frac{\gamma_g}{\epsilon_{ef}} + ik_x \frac{\epsilon_{12}}{\epsilon_{11}^2 + \epsilon_{12}^2} = 0. \quad (9)$$

Figure 2(a) depicts the plasmons dispersion ( $\omega = \omega_{k_x}^{\text{SPP}}$ ) for a lossless magnetized plasma with  $\omega_0 = 0.5\omega_p$ . In contrast to

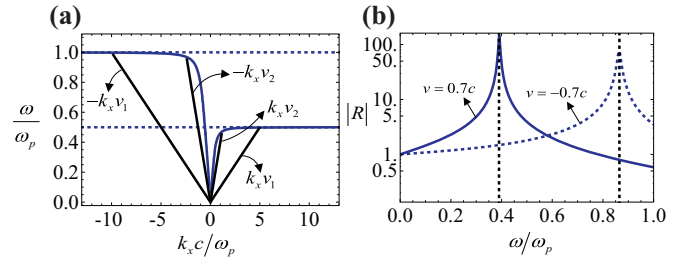


FIG. 2. (a) Dispersion diagrams of the edge (surface) plasmons propagating at an interface between air and a magnetized plasma with  $\omega_0 = 0.5\omega_p$  (blue thick lines). The plasmon resonance occurs at  $\omega = \omega_+$ , for  $k_x > 0$ , and  $\omega = \omega_-$  for  $k_x < 0$ . The thin black lines represent the curves  $\omega = k_x v$  for the velocities  $v_1 = \pm 0.1c$  and  $v_2 = \pm 0.4c$ . Their intersection with the dispersion diagram determines the main emission channels in the Cherenkov problem. (b) Amplitude of the reflection coefficient (in a logarithmic scale) for  $v = \pm 0.7c$ . The vertical gridlines correspond approximately to  $\omega/\omega_p \approx 0.78\omega_+$  (curve  $v = 0.7c$ ) and  $\omega/\omega_p \approx 0.87\omega_-$  (curve  $v = -0.7c$ ). The collision frequency was taken equal to  $\Gamma = 0.01\omega_p$ .

the bulk states, the SPPs dispersion is strongly asymmetric due to the inhomogeneity of space (which breaks the parity symmetry) and the nonreciprocity inherent to gyrotropic material. In particular, the plasmon resonance, i.e., the asymptotic value reached when  $k_x \rightarrow \pm\infty$ , depends on the direction of propagation of the plasmons. It is given by [40]

$$\lim_{k_x \rightarrow \pm\infty} \omega_{k_x}^{\text{SPP}} \equiv \omega_{\pm} = \frac{1}{2} (\mp \omega_0 + \sqrt{2\omega_p^2 + \omega_0^2}). \quad (10)$$

In the Cherenkov problem, the wave number along  $x$  and the frequency are linked by  $k_x = \omega/v$ . Hence a natural (surface or bulk) mode of the system can be excited by the moving charges when the following selection rule is satisfied for some  $k_x$ :

$$\omega_{k_x} = k_x v. \quad (11)$$

Here,  $\omega_{k_x}$  represents the dispersion of the relevant modes (e.g., for the SPP waves  $\omega_{k_x} = \omega_{k_x}^{\text{SPP}}$ ). Figure 2(a) depicts the lines  $\omega = \pm k_x v$  for two different values of the charges velocity. As seen, when  $v > 0$ , they intersect the plasmon dispersion at some point with  $\omega \approx \omega_+$ , whereas if  $v < 0$ , they intersect the plasmon dispersion at some point with  $\omega \approx \omega_-$ . Thus the Cherenkov emission spectrum may be strongly asymmetric. For positive velocities it will be peaked near  $\omega \approx \omega_+$ , whereas for negative velocities, it will be peaked near  $\omega \approx \omega_-$ . The moving charges can also be coupled to bulk modes with dispersion  $\omega_k^{\text{bulk}}$ . However, as previously discussed,  $\omega_k^{\text{bulk}}$  is an even function of  $k_x$ , and hence does not lead to any emission asymmetry.

In the Cherenkov problem, the amplitude of the scattered fields is determined by the reflection coefficient  $R(\omega, k_x)|_{k_x=\omega/v}$ . Figure 2(b) depicts the reflection coefficient amplitude as a function of frequency. Consistent with Fig. 2(a), the reflection coefficients are highly asymmetric being peaked precisely at the frequencies at which the selection rule (11) is satisfied [vertical gridlines in Fig. 2(b)], i.e., relatively near  $\omega_{\pm}$  depending on the sign of the electrons velocity.

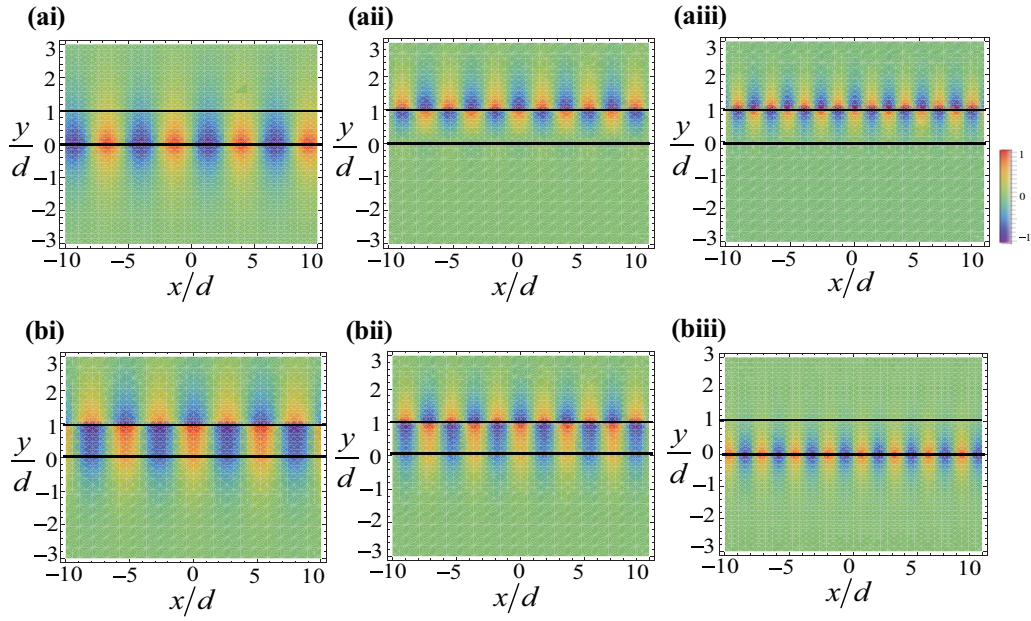


FIG. 3. Real part of the magnetic field emission spectrum  $H_z(x, y, \omega)$  (in arbitrary units) for an array of moving charges in the vicinity of a magnetized plasma with  $\omega_0 = 0.5\omega_p$ ,  $\omega_p d/c = 1$ , and  $\Gamma = 0^+$ . (a)  $v = 0.4c$  and (i)  $\omega = 0.94\omega_+$ , (ii)  $0.7\omega_-$ , (iii)  $0.97\omega_-$ . (b) Similar to (a) but for  $v = -0.4c$ .

The previous result suggests that the moving charges can efficiently excite the surface plasmons. Depending on the sign of the velocity, the spectrum of the emitted Cherenkov radiation will be peaked at the plasmon resonance  $\omega_+$  or  $\omega_-$ . To demonstrate the plasmon excitation and the spectral asymmetry of the emitted radiation, we depict in Fig. 3 the frequency domain magnetic field [Eq. (4)] calculated at the frequencies  $\omega = 0.94\omega_+$  [Figs. 3(ai) and 3(bi)],  $\omega = 0.7\omega_-$  [Figs. 3(aii) and 3(bii)] and  $\omega = 0.97\omega_-$  [Figs. 3(aiii) and 3(biii)]. The plots in Fig. 3(a) [Fig. 3(b)] correspond to positive (negative) values of the charges velocity. The thin horizontal black line (on the top) represents the trajectory of the charges and the thick horizontal black line the interface. As seen, the SPPs are strongly excited in the examples of Figs. 3(ai) [ $\omega \approx \omega_+$  and  $v > 0$ ] and 3(biii) [ $\omega \approx \omega_-$  and  $v < 0$ ] such that the magnetic field is concentrated near the interface  $y = 0$ . For frequencies far from the plasmon resonances,  $\omega_+$  or  $\omega_-$  [Figs. 3(aii) and 3(bii)], the SPP emission is not observed, and the fields are concentrated near the trajectory of the moving charges.

Figure 4 shows a density plot of the instantaneous magnetic field radiated by the moving charges for different values of the velocity and material loss. The magnetic field was calculated using Eq. (6) for  $t = 0$ , which corresponds to the charges position  $x = 0$ . The time-domain simulation confirms that the SPP waves are indeed the main Cherenkov emission channels. Notably, a strongly asymmetric Cherenkov radiation is observed in the plots with opposite velocity signs [e.g., Figs. 4(ai) and 4(aii)]. In the case of stronger material absorption [Figs. 4(bi) and 4(bii)], the emitted SPPs are evidently damped after propagating a few guided wavelengths.

Figure 5(a) depicts the normalized power spectral density  $G$  [Eq. (7)] for  $\Gamma = 0.01\omega_p$  and  $\omega_0 = 0.5\omega_p$ . Clearly, the emission spectrum is highly asymmetric being peaked near  $\omega_{\pm}$  [vertical gridlines in Fig. 5(a)] depending on the sign of

the electrons velocity. This property is explained by the fact that the density of (plasmon) states diverges at the frequencies determined by  $\lim_{k_x \rightarrow \pm\infty} \omega_{k_x}^{\text{SPP}}$ , and further underscores the relevance of plasmons in the Cherenkov problem. The “stopping power” [Eq. (6)] is represented in Fig. 5(b) for different values of the distance  $d$ . For increasing values of  $d$ , the stopping power decreases because the coupling between

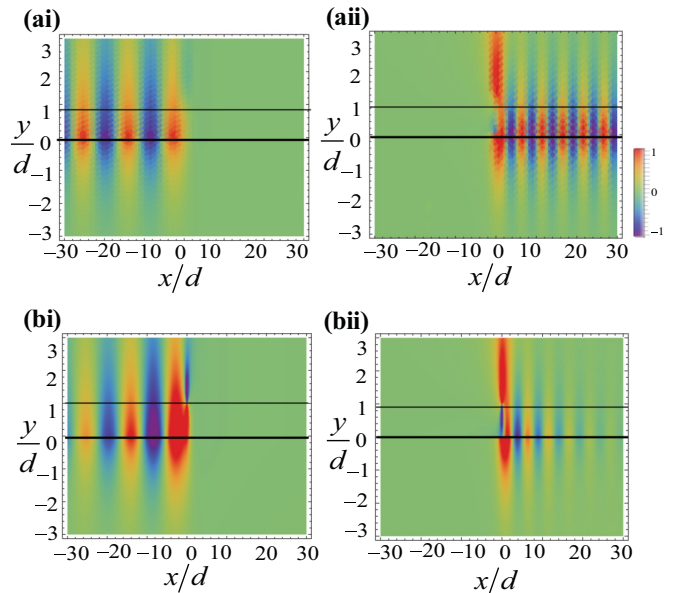


FIG. 4. Time snapshot ( $t = 0$ ) of the magnetic field  $H_z$  (in arbitrary units) for an array of moving charges in the vicinity of a magnetized plasma with cyclotron frequency  $\omega_0 = 0.5\omega_p$  and for  $\omega_p d/c = 1$ . (ai)  $v = 0.7c$ ,  $\Gamma = 0.001\omega_p$  and (aii)  $v = -0.7c$ ,  $\Gamma = 0.001\omega_p$ . (b) Similar to (a) but with  $\Gamma = 0.1\omega_p$ .

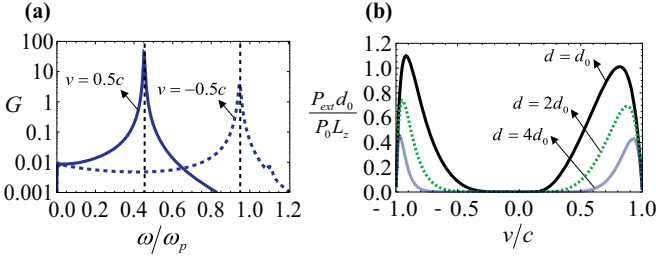


FIG. 5. (a) Normalized power spectral density  $G$  as a function of the normalized frequency for  $\omega_p d/c = 1$ . The vertical gridlines indicate the points that satisfy the selection rule (11), relatively near the plasmon resonances  $\omega \approx \omega_{\pm}$ . (b) Normalized stopping power  $P_{ext}$  as a function of the charge velocity  $v$ , for  $d = d_0$ ,  $d = 2d_0$ , and  $d = 4d_0$  with  $\omega_p d_0/c = 1$ .

the self-field of the moving charges and the plasmons is weaker. As expected, the stopping power is typically larger for more energetic beams (with a larger  $v$ ). However, after some velocity threshold value the stopping power drops sharply. The reason is that for large velocities the intersection of the line  $\omega = k_x v$  with the plasmons dispersion  $\omega_{k_x}^{SPP}$  occurs at points more distant from the “flat” parts of  $\omega_{k_x}^{SPP}$  [see Fig. 2(a)], where the density of states is smaller.

### B. Weyl semimetal

As a second example, we consider a linear array of charges moving in a vacuum above a Weyl semimetal half-space. It has been suggested that pyrochlore iridates of the generic form  $A_2\text{Ir}_2\text{O}_7$ , with A either yttrium or a lanthanide element, may be topological semimetals [15,16]. The topological properties of a Weyl semimetal result in an anomalous Hall current (chiral anomaly) and create a gyrotropic (nonreciprocal) electromagnetic response, even *without* an external magnetic bias [17]. Thus Weyl semimetals may have a spontaneous nonreciprocal response due to magnetic ordering [15]. There are other naturally available materials with a spontaneous nonreciprocal response, e.g., some antiferromagnets [41–46].

Following Ref. [17], a Weyl semimetal has a permittivity tensor of the form  $\bar{\epsilon} = \epsilon_t \mathbf{1} + i\epsilon_g \hat{\mathbf{z}} \times \mathbf{1}$  with permittivity components

$$\epsilon_t = \epsilon_{\infty} \left( 1 - \frac{\omega_p^2}{\omega^2} \right), \quad \epsilon_g = \epsilon_{\infty} \frac{\omega_b}{\omega}, \quad (12)$$

where  $\epsilon_{\infty}$  is the high-frequency permittivity,  $\omega_p$  denotes the bulk plasma frequency, and  $\omega_b$  is a parameter with units of frequency which is nontrivial for topological Weyl semimetals [17]. Here, the  $z$  axis is taken as the direction of the wave vector  $\mathbf{b}$  that links the two Weyl points in the 1<sup>st</sup> Brillouin zone [17]. Figure 1 shows the band diagram of a bulk Weyl semimetal for the case  $\epsilon_{\infty} = 1$  and  $\omega_b = 0.5\omega_p$ . Similar to the magnetized plasma case, the band diagram exhibits spectral symmetry.

The plasmon dispersion diagram is plotted in Fig. 6(a) for the parameters  $\epsilon_{\infty} = 1$  and  $\omega_b = 0.5\omega_p$  showing a behavior qualitatively similar to that of the magnetized plasma case.

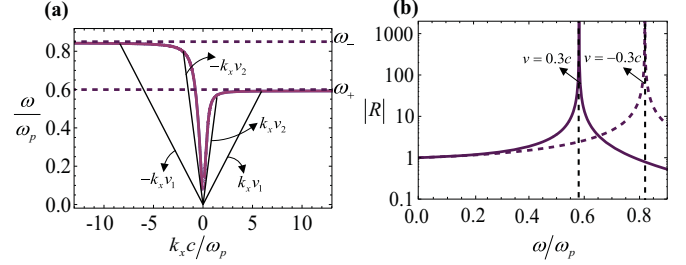


FIG. 6. (a) Dispersion diagrams of the edge (surface) plasmons propagating at an interface between air and a Weyl semimetal (purple thick lines). The plasmon resonance occurs at  $\omega_+ \approx 0.59\omega_p$ , for  $k_x > 0$ , and  $\omega_- \approx 0.84\omega_p$ , for  $k_x < 0$ . The thin black lines represent the curves  $\omega = k_x v$  for the velocities  $v_1 = \pm 0.1c$  and  $v_2 = \pm 0.4c$ . (b) Amplitude of the reflection coefficient (in a logarithmic scale) for  $v = \pm 0.3c$ . The vertical gridlines correspond approximately to  $\omega \approx 0.99\omega_+$  (curve  $v = 0.3c$ ) and  $\omega \approx 0.98\omega_-$  (curve  $v = -0.3c$ ).

Now, the dispersion curves saturate at the plasmon resonances

$$\lim_{k_x \rightarrow \pm\infty} \omega_{k_x}^{SPP} \equiv \omega_{\pm} = \frac{\epsilon_{\infty}}{2(1 + \epsilon_{\infty})} \times \left( \mp \omega_b + \sqrt{\frac{1 + \epsilon_{\infty}}{\epsilon_{\infty}} 4\omega_p^2 + \omega_b^2} \right). \quad (13)$$

Similar to Fig. 2(b), the reflection coefficient is typically peaked near the plasmon resonances  $\omega_{\pm}$  [see Fig. 6(b)].

Furthermore, the magnetic field emission spectrum (not shown) and the instantaneous magnetic field (Fig. 7) have features qualitatively very similar to the magnetized plasma examples. They confirm the selective emission of plasmons with spectrum concentrated near  $\omega_{\pm}$ , depending if the pencil beam travels along the  $+x$  or  $-x$  direction, and that plasmons are typically the main emission channels.

The power spectral density  $G$  [Fig. 8(a)] and the stopping power [Fig. 8(b)] also have features qualitatively similar to the magnetized plasma case. For example, the power spectral density is resonant near  $\omega_{\pm}$ , depending on the sign of  $v$ . However, it must be highlighted that the nonreciprocal response of the Weyl semimetal is spontaneous and hence it does not require an external magnetic bias.

In the previous examples, it was assumed that  $\epsilon_{\infty} = 1$  but it may be more realistic to take  $\epsilon_{\infty} > 1$  in the material

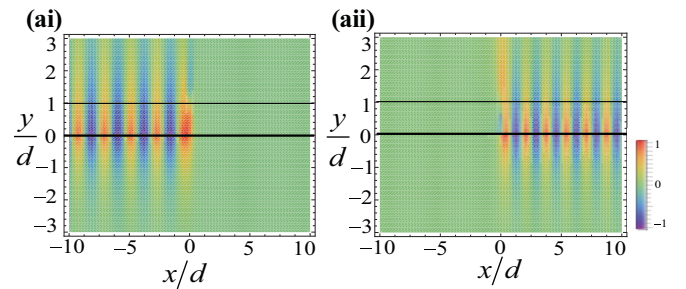


FIG. 7. Time snapshot ( $t = 0$ ) of the magnetic field  $H_z$  (in arbitrary units) for an array of moving charges in the vicinity of a Weyl semimetal with  $\epsilon_{\infty} = 1$ ,  $\omega_b = 0.5\omega_p$ , and  $\omega_p d/c = 1$ . (ai)  $v = 0.7c$  and (aii)  $v = -0.7c$ .

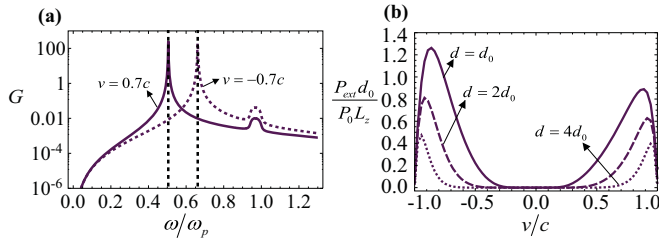


FIG. 8. (a) Normalized power spectral density  $G$  as a function of the normalized frequency for  $\omega_p d/c = 1$ . The vertical gridlines indicate the points that satisfy the selection rule (11). (b) Normalized stopping power  $P_{\text{ext}}$  as a function of the charge velocity  $v$ , for  $d = d_0$ ,  $d = 2d_0$ , and  $d = 4d_0$  with  $\omega_p d_0/c = 1$ . In the simulations, we used  $\varepsilon_\infty = 1$  and  $\omega_b = 0.5\omega_p$ .

response model [17]. The reason for using  $\varepsilon_\infty = 1$  is that in the Cherenkov problem the high-frequency response is of a crucial importance. For example, taking  $\varepsilon_\infty \neq 1$  when the charged particles move inside a material leads to divergences and to an infinite stopping power [26]. Hence, usually, it is essential to consider realistic dispersive models that fully satisfy the Kramers-Kronig relations with  $\varepsilon_\infty = 1$  [20]. In our case, the beam of charges moves outside the material and in this situation the distance  $d$  to the material provides a natural cutoff, which avoids the aforementioned divergences. However, taking  $\varepsilon_\infty \neq 1$  may overestimate the amount of radiation emitted in the form of bulk states. With this note of caution, we represent in Fig. 9 the instantaneous magnetic field calculated for different values of  $\varepsilon_\infty$ . As seen, for increasingly larger values of  $\varepsilon_\infty$  the amount of radiation emitted in the form of bulk states increases, and the overall importance of the surfaces plasmons decreases. Indeed, a well-defined Cherenkov cone becomes visible in the region  $y < 0$  when  $\varepsilon_\infty \neq 1$ . The cone becomes more tilted as  $\varepsilon_\infty$

increases. Evidently, even when  $\varepsilon_\infty \neq 1$ , the surface plasmons remain the main emission channels in the spectral windows near  $\omega_\pm$ .

#### IV. ANALYTICAL SOLUTION FOR THE STOPPING POWER

If the charge velocity satisfies  $|v| \ll c$ , and, if in addition the electrons move sufficiently close to the surface of the topological material ( $\omega_p d/c \ll 1$ ), the effects of time retardation can be neglected. In such a case, the light-matter interactions are essentially quasistatic and in particular it is possible to characterize the power extracted from the moving beam using a quasistatic approximation.

To this end, we rely on the formalism of Appendix B, which gives the stopping power in terms of the electromagnetic modes of the system [Eq. (B10)]. In the quasistatic limit, the main radiation channels are determined by the surface plasmons. For simplicity, we restrict the analysis to the case of a gyrotropic material with dispersion as in Eq. (8). It was recently shown that the (short-wavelength) surface plasmons at an air-gyrotropic material interface are of the form  $\mathbf{E}_\mathbf{k} \approx -\nabla\phi_\mathbf{k}$ ,  $\mathbf{H}_\mathbf{k} \approx 0$  with

$$\phi_\mathbf{k} = A_\mathbf{k} e^{i\mathbf{k}\cdot\mathbf{r}} \begin{cases} e^{-k_\parallel y}, & y > 0 \\ e^{+k_\parallel y}, & y < 0 \end{cases}, \quad (14)$$

with  $\mathbf{k} = (k_x, 0, k_z)$  the transverse wave vector (parallel to the interface),  $k_\parallel = \sqrt{k_x^2 + k_z^2}$ ,  $\tilde{k}_\parallel = \sqrt{k_x^2 + \frac{\varepsilon_a}{\varepsilon_t} k_z^2}$ , and  $A_\mathbf{k}$  a normalization constant. Furthermore, the dispersion of the short-wavelength plasmons satisfies (the formulas of this article differ slightly from those of Ref. [40] due to a different

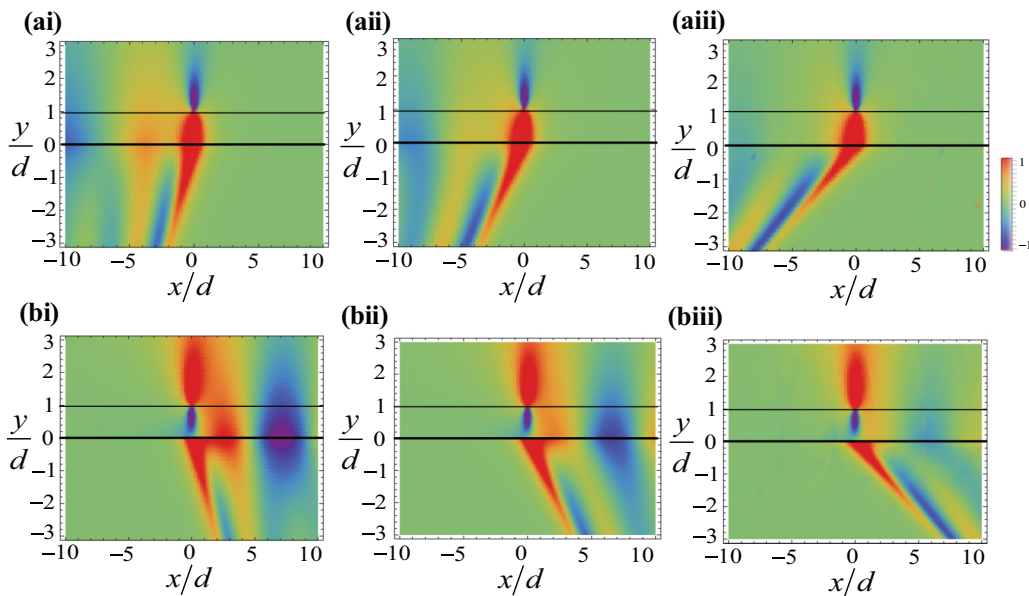


FIG. 9. Time snapshot ( $t = 0$ ) of the magnetic field  $H_z(x, y, t)$  (in arbitrary units) radiated by a linear array of moving charges for  $\omega_b = 0.5\omega_p$  and  $\omega_p d/c = 1$ . (a) The charges velocity is  $v = 0.7c$  and the high-frequency permittivity is (i)  $\varepsilon_\infty = 3$ , (ii) 5, and (iii) 13. (b) Similar to (a) but with  $v = -0.7c$ .

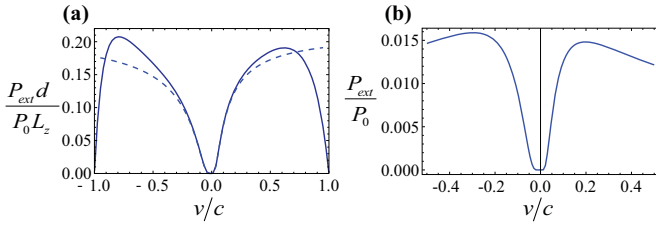


FIG. 10. (a) Comparison between the exact stopping power (solid line) and the stopping power obtained with the quasistatic approximation [Eq. (16)] (dashed line) for a “pencil” beam. (b) Stopping power obtained with the quasistatic approximation [Eq. (17)] for a “pointlike” beam. In both plots we use  $\omega_p d/c = 0.1$  and  $\omega_0/\omega_p = 0.4$ .

choice of the coordinate axes) [40]

$$\omega_{\mathbf{k}} \equiv \omega_{\varphi} = -\frac{\omega_0}{2} \cos \varphi + \sqrt{\frac{\omega_p^2}{2} + \frac{\omega_0^2}{4}(1 + \sin^2 \varphi)}, \quad (15)$$

with  $\varphi$  the angle of the SPP wave vector  $\mathbf{k}$  with respect to the  $x$  axis. As discussed in detail in Ref. [40], one has  $\lim_{k \rightarrow +\infty} \omega_{\mathbf{k}}^{\text{SPP}}(\cos \varphi, 0, \sin \varphi) \equiv \omega_{\varphi}$  and in particular  $\omega_{\varphi=0, \pi} = \omega_{\pm}$ . Thus the quasistatic approximation describes the plasmon resonances with a large wave vector. The plasmon resonances are direction dependent due to the magnetic bias.

In Appendix C, we use the quasistatic model to determine the stopping power. For the case of a pencil beam, it is found that

$$\frac{P_{\text{ext}}}{L_z} = P_0 \frac{4\pi \frac{\omega_{\pm}}{c} e^{-2\frac{\omega_{\pm} y_0}{v}}}{[1 + \partial_{\omega}(\varepsilon_r \omega) - \partial_{\omega}(\varepsilon_g \omega) \text{sgn}(v)]_{\omega=\omega_{\pm}}}, \quad (16)$$

with  $P_0 = \frac{n_z^2 e^2}{4\pi \varepsilon_0} c$ . The “+” sign (“−” sign) is chosen for positive (negative) velocities. A comparison between this quasistatic result and the exact theory of Sec. II is reported in Fig. 10(a). As seen, the agreement is excellent for velocities  $|v|/c < 0.3$ . For large velocities, the quasistatic approximation breaks down because the effects of time retardation become relevant (as previously discussed, for large velocities, the excited plasmons have long wavelengths, i.e., a small  $\mathbf{k}$ ; hence they cannot be modeled by Eq. (15), which describes the dispersion of the short-wavelength plasmons).

Furthermore, in Appendix C, we also determine the stopping power for the case of a “pointlike” beam described by the current density  $\mathbf{j}_e(x, y, t) = -ev\delta(z)\delta(y - y_0)\delta(x - vt)\hat{\mathbf{x}}$  (this current density corresponds to a single moving electron). The quasistatic solution of this fully three-dimensional radiation problem is

$$P_{\text{ext}} = P_0 \int_{v \cos \varphi > 0} d\varphi \frac{\omega_{\varphi}^2 y_0^2}{|c v \cos \varphi|} a_{\varphi} e^{-2\frac{\omega_{\varphi}}{v \cos \varphi} y_0}, \quad (17)$$

where the normalization factor is now  $P_0 = \frac{e^2 c}{4\pi \varepsilon_0} \frac{1}{y_0}$  and  $y_0 = d$ . In the above,  $\omega_{\varphi}$  is defined by Eq. (15) and  $a_{\varphi} = \varepsilon_0 k_{\parallel} |A_{\mathbf{k}}|^2$  with  $|A_{\mathbf{k}}|^2$  given by Eq. (C3). The integration range is over  $-\pi/2 < \varphi < \pi/2$  for positive velocities and over  $\pi/2 < \varphi < 3\pi/2$  for negative velocities. The computed stopping power is shown in Fig. 10(b) as a function of the charge velocity. As seen, the results are qualitatively similar to the pencil

beam case and exhibit a pronounced asymmetry such that the stopping power depends strongly on the sign of the velocity.

## V. CONCLUSIONS

In this work, it was demonstrated that the main radiation channels for the Cherenkov energy emitted by charged particles moving near to a topological material half-space are the edge states (plasmons) supported by the interface. It was shown that the emission spectrum is highly asymmetric, being peaked near a plasmon resonance that depends on the sign of the charge velocity. The theory was applied to magnetized plasmas and Weyl semimetals. In particular, it was found that Weyl semimetals offer the opportunity to obtain strongly asymmetric Cherenkov emissions with no biasing magnetic field. The platforms described in this work offer the possibility to discriminate particles travelling in opposite directions of space in a simple manner, which can have applications in particle detection and biomedicine.

## ACKNOWLEDGMENTS

This work is supported in part by Fundação para a Ciência e a Tecnologia Grant No. PTDC/EEI-TEL/4543/2014 and by Instituto de Telecomunicações under project UID/EEA/50008/2017. F.R.P. acknowledges financial support by Fundação para a Ciência e a Tecnologia (FCT) under the Post-Doctoral fellowship SFRH/BPD/108823/2015.

## APPENDIX A: EFFECT OF THE MAGNETIC FIELD ON THE MOVING CHARGES

In this appendix, we discuss the influence of the static magnetic field on the moving charges. It is supposed that the moving particles have the same charge (in absolute value) as the electron, but not necessarily the same mass, e.g., the moving charges may be protons [47]. A moving charge will follow a circular trajectory under the action of a uniform magnetic field  $B_0$ , with cyclotron radius  $R = |m v / (q B_0)|$  (the magnetic field is assumed perpendicular to the velocity  $v$ ). It can be readily checked that the vertical deflection  $\Delta$  suffered by the moving charges as they travel the distance  $D$  along the horizontal direction is  $\Delta \approx D^2 / (2R)$ . In order that the vertical deflection is negligible, it is necessary that  $\Delta \ll d$ , with  $d$  the distance to the interface, let us say  $\Delta < d/4$ , or equivalently  $D < \sqrt{Rd/2}$ . Using the formula of the cyclotron radius we get

$$\frac{D}{d} < \sqrt{\frac{1}{2} \frac{m}{m^*} \frac{v}{|\omega_0| d}}, \quad (A1)$$

where  $\omega_0 = -q B_0 / m^*$  is the cyclotron frequency of the gyrotropic material. This condition may be rewritten as

$$\frac{D}{d} < \sqrt{\frac{m}{m^*}} \sqrt{\frac{\omega_p}{2|\omega_0|}} \sqrt{\frac{v}{c} \frac{c}{\omega_p d}}. \quad (A2)$$

In the simulations of the main text, the last square root has values on the order of 1. Hence, to have a large travelling distance  $D/d \gg 1$  with a small perturbation of the charge trajectory, one either needs (i) a weak magnetic field

( $|\omega_0|/\omega_p \ll 1$ ), or alternatively (ii) a large value for  $m/m^*$ . The latter option is feasible when the moving charges are protons [47]. Indeed, in such a case  $m = 1835m_e$ , with  $m_e$  the rest mass of the electron. Furthermore, the effective mass of the electrons that determine the gyrotropic response can be on the order of  $m^* = 0.025m_e$  for narrow gap semiconductors such as InSb [35]. Thus the factor  $\sqrt{m/m^*}$  can be as large as 271 for protons, and thereby with heavy charged particles it may be possible to neglect the trajectory deflection, even with a large static magnetic field.

## APPENDIX B: MODAL EXPANSION OF THE RADIATED FIELDS AND STOPPING POWER

In this appendix, we obtain explicit formulas for the fields emitted by a moving charge distribution and for the stopping power in terms of a modal expansion [27,48,49]. The derived formulas are exact and the only assumption is that the material loss is negligible.

To begin with, we determine the fields emitted by a generic current density. For simplicity, we use six-vector notations and denote the electromagnetic fields as  $\mathbf{f}(\mathbf{r}, t) = (\mathbf{E} \ \mathbf{H})^T$  and the excitation currents as  $\mathbf{j}(\mathbf{r}, t) = (\mathbf{j}_e \ \mathbf{j}_m)^T$ . Here,  $\mathbf{j}_e$  is the instantaneous electric current density and  $\mathbf{j}_m$  is the instantaneous magnetic current density, which will be taken identical to zero. Furthermore, we introduce a  $6 \times 6$  frequency-domain Green tensor (with a time-harmonic variation  $e^{-i\omega t}$ ) defined as the solution of [48,49]

$$\hat{N} \cdot \bar{\mathbf{G}}(\mathbf{r}, \mathbf{r}_0, \omega) = \omega \mathbf{M}(\mathbf{r}, \omega) \cdot \bar{\mathbf{G}}(\mathbf{r}, \mathbf{r}_0, \omega) + i\mathbf{1}\delta(\mathbf{r} - \mathbf{r}_0) \quad (\text{B1})$$

with  $\hat{N} = \begin{pmatrix} 0 & i\nabla \times \mathbf{1}_{3 \times 3} \\ -i\nabla \times \mathbf{1}_{3 \times 3} & 0 \end{pmatrix}$ ,  $\mathbf{1}$  the identity matrix of dimension six, and  $\mathbf{M} = \begin{pmatrix} \epsilon_0 \bar{\epsilon}(\mathbf{r}, \omega) & 0 \\ 0 & \mu_0 \mathbf{1}_{3 \times 3} \end{pmatrix}$  the material matrix that determines the electromagnetic response of the relevant materials.

Let  $\mathbf{j}_\omega(\mathbf{r})$  be the Fourier transform of the generalized current vector  $\mathbf{j}(\mathbf{r}, t)$ . Then, the Fourier transform of the fields satisfies

$$\mathbf{f}_\omega(\mathbf{r}) = \int d^3\mathbf{r}' \bar{\mathbf{G}}(\mathbf{r}, \mathbf{r}', \omega) \cdot \mathbf{j}_\omega(\mathbf{r}'). \quad (\text{B2})$$

In the limit of vanishing material loss, the Green function has the modal expansion [48,49]

$$\bar{\mathbf{G}} = \frac{i}{2} \sum_n \frac{1}{\omega_n - \omega} \mathbf{f}_n(\mathbf{r}) \otimes \mathbf{f}_n^*(\mathbf{r}_0). \quad (\text{B3})$$

Here,  $\mathbf{f}_n(\mathbf{r})$  represents a generic electromagnetic mode with oscillation frequency  $\omega_n$  and is normalized as ( $V$  stands for the volume of the relevant region)  $\frac{1}{2} \int_V d^3\mathbf{r} \mathbf{f}_n^*(\mathbf{r}) \cdot \frac{\partial}{\partial \omega} [\omega \mathbf{M}(\mathbf{r}, \omega)]_{\omega=\omega_n} \cdot \mathbf{f}_n(\mathbf{r}) = 1$ . The summation is over all the electromagnetic modes with either positive, zero, or negative frequencies [48,49].

For the geometry of interest [Fig. 1(a)], the modes are of the form  $\mathbf{f}_n(\mathbf{r}) \rightarrow \frac{1}{\sqrt{A_{\text{tot}}}} \mathbf{F}_{n\mathbf{q}}(y) e^{i\mathbf{q}\cdot\mathbf{r}}$  with  $\mathbf{q} = (q_x, 0, q_z)$  the transverse wave vector (which is a good quantum number due to the translational invariance along the  $x$  and  $z$  directions) and  $A_{\text{tot}}$  the transverse area (section parallel to the interface). Taking into account that the modes form a continuum

( $A_{\text{tot}} \rightarrow \infty$ ), it follows that

$$\bar{\mathbf{G}} = \frac{i}{2} \sum_n \frac{1}{(2\pi)^2} \int d^2\mathbf{q} \frac{1}{\omega_{n\mathbf{q}} - \omega} \mathbf{F}_{n\mathbf{q}}(y) \otimes \mathbf{F}_{n\mathbf{q}}^*(y_0) e^{i\mathbf{q}\cdot(\mathbf{r}-\mathbf{r}_0)} \quad (\text{B4})$$

with  $d^2\mathbf{q} = dq_x dq_z$  and the envelopes  $\mathbf{F}_{n\mathbf{q}}$  normalized as

$$\frac{1}{2} \int dy \mathbf{F}_{n\mathbf{q}}^*(y) \cdot \frac{\partial}{\partial \omega} [\omega \mathbf{M}(y, \omega)]_{\omega=\omega_{n\mathbf{q}}} \cdot \mathbf{F}_{n\mathbf{q}}(y) = 1. \quad (\text{B5})$$

Hence, the radiated field in the spectral domain is

$$\mathbf{f}_\omega(\mathbf{r}) = \frac{i}{2} \sum_n \frac{1}{(2\pi)^2} \int d^2\mathbf{q} \frac{1}{\omega_{n\mathbf{q}} - \omega} \mathbf{F}_{n\mathbf{q}}(y) \times \int d^3\mathbf{r}' \mathbf{F}_{n\mathbf{q}}^*(y') e^{i\mathbf{q}\cdot(\mathbf{r}-\mathbf{r}')} \cdot \mathbf{j}_\omega(\mathbf{r}'). \quad (\text{B6})$$

Let us now suppose that the time-dependence of the current is of the form  $\mathbf{j} = \mathbf{j}_0(y, z)\delta(x - vt)$  as in the Cherenkov problem. Then,  $\mathbf{j}_\omega = \frac{1}{|v|} \mathbf{j}_0(y, z) e^{ik_x x}$ , where  $k_x = \omega/v$ . From here, we can write (after carrying out the integration in  $x'$ )

$$\mathbf{f}_\omega(\mathbf{r}) = \frac{i}{2|v|} \sum_n \frac{1}{2\pi} \int d^2\mathbf{q} e^{iq_x x} \delta\left(q_x - \frac{\omega}{v}\right) \frac{1}{\omega_{n\mathbf{q}} - \omega} \mathbf{F}_{n\mathbf{q}}(y) \times \int dy' dz' \mathbf{F}_{n\mathbf{q}}^*(y') \cdot \mathbf{j}_0(y', z') e^{iq_z(z-z')}. \quad (\text{B7})$$

Calculating the inverse Fourier transform in time  $\mathbf{f} = \frac{1}{2\pi} \int d\omega \mathbf{f}_\omega e^{-i\omega t}$  (the integration contour is slightly above the real-frequency axis), we obtain the following modal expansion for the radiated field:

$$\mathbf{f}(\mathbf{r}, t) = \frac{i}{2} \sum_n \frac{1}{(2\pi)^2} \int d^2\mathbf{q} e^{iq_x(x-vt)} \frac{1}{\omega_{n\mathbf{q}} - q_x v - i0^+} \times \mathbf{F}_{n\mathbf{q}}(y) \int dy' dz' \mathbf{F}_{n\mathbf{q}}^*(y') \cdot \mathbf{j}_0(y', z') e^{iq_z(z-z')}. \quad (\text{B8})$$

From the above result, one may write the stopping power ( $P_{\text{ext}} = -\int dV \mathbf{j} \cdot \mathbf{f}$ ) in terms of the electromagnetic modes. Using again  $\mathbf{j} = \mathbf{j}_0(y, z)\delta(x - vt)$  and noting that  $\mathbf{j}_0(y, z)$  is real-valued, one obtains

$$P_{\text{ext}} = \frac{-i}{2} \sum_n \frac{1}{(2\pi)^2} \int d^2\mathbf{q} \frac{1}{\omega_{n\mathbf{q}} - q_x v - i0^+} \times \left| \int dy dz e^{iq_z z} \mathbf{F}_{n\mathbf{q}}(y) \cdot \mathbf{j}_0(y, z) \right|^2. \quad (\text{B9})$$

Clearly, the stopping power must be a real-valued number. On the other hand, the integrand is pure imaginary except for the contributions of the  $i0^+$  term near the poles. Using  $\frac{1}{x-i0^+} = \text{PV} \frac{1}{x} + i\pi\delta(x)$  (PV stands for the ‘‘principal value’’), we find that

$$P_{\text{ext}} = \frac{1}{4\pi} \sum_{\omega_{n\mathbf{q}} > 0} \int d^2\mathbf{q} \delta(\omega_{n\mathbf{q}} - q_x v) \times \left| \int dy dz e^{iq_z z} \mathbf{F}_{n\mathbf{q}}(y) \cdot \mathbf{j}_0(y, z) \right|^2. \quad (\text{B10})$$

Consistent with the selection rule (11) only modes that satisfy  $\omega_{n\mathbf{q}} = q_x v$  contribute to the stopping power. The

summation was restricted to positive frequency modes because the modes with  $\omega_{n\mathbf{q}} < 0$  give the same contribution as the modes with  $\omega_{n\mathbf{q}} > 0$ .

### APPENDIX C: STOPPING POWER IN A QUASISTATIC APPROXIMATION

In this Appendix, we derive explicit analytical formulas for the stopping power using the quasistatic approximation discussed in Sec. IV. We analyze both the cases of a pencil beam and of a pointlike beam.

#### 1. Pencil beam

We consider first a pencil beam with  $\mathbf{j}_0(y, z) = -en_z v \delta(y - y_0) \hat{\mathbf{u}}_1$  with  $\hat{\mathbf{u}}_1 = \begin{pmatrix} \hat{\mathbf{x}} \\ 0 \end{pmatrix}$ . Within the quasistatic approximation, there is a single branch of positive-frequency modes and hence the summation over  $n$  can be dropped in Eq. (B10). Denoting the wave vector of the surface plasmons with the symbol  $\mathbf{k}$  ( $n\mathbf{q} \rightarrow \mathbf{k}$ ), it follows that the stopping power is

$$\frac{P_{\text{ext}}}{L_z} = \frac{(evn_z)^2}{2} \int d^2\mathbf{k} \delta(\omega_{\mathbf{k}} - k_x v) \delta(k_z) |\mathbf{F}_{\mathbf{k}}(y_0) \cdot \hat{\mathbf{u}}_1|^2. \quad (\text{C1})$$

Furthermore, from Eq. (15), one has  $\omega_{\mathbf{k}} = \omega_+$  for  $k_x > 0$  and  $k_z = 0$  and  $\omega_{\mathbf{k}} = \omega_-$  for  $k_x < 0$  and  $k_z = 0$ . This observation leads to

$$\frac{P_{\text{ext}}}{L_z} = \frac{(en_z)^2 |v|}{2} |\mathbf{F}_{\mathbf{k}}(y_0) \cdot \hat{\mathbf{u}}_1|^2 \Big|_{\substack{k_x = \omega_{\pm}/v \\ k_z = 0}}, \quad (\text{C2})$$

where the “+” sign (“−” sign) is chosen for positive (negative) velocities. To proceed, we use the fact that within the quasistatic approximation the fields have an electrostatic nature such that  $\mathbf{F}_{\mathbf{k}} \approx \begin{pmatrix} \mathbf{E}_{\mathbf{k}} \\ 0 \end{pmatrix} \approx \begin{pmatrix} -\nabla\phi_{\mathbf{k}} \\ 0 \end{pmatrix}$  [40], with  $\phi_{\mathbf{k}}$  given by Eq. (14). The constant  $A_{\mathbf{k}}$  is determined by the normalization condition (B5). It can be written explicitly as (the difference

compared to Ref. [40] is again due to the different coordinate system) [40]

$$|A_{\mathbf{k}}|^2 = \frac{2}{\varepsilon_0} \left[ k_{\parallel} + \frac{1}{2\tilde{k}_{\parallel}} (\partial_{\omega}(\varepsilon_r \omega) (\tilde{k}_{\parallel}^2 + k_x^2) + \partial_{\omega}(\varepsilon_a \omega) k_z^2 - \partial_{\omega}(\varepsilon_g \omega) 2k_x \tilde{k}_{\parallel}) \right]^{-1}. \quad (\text{C3})$$

Using these results to simplify (C2), one obtains

$$\frac{P_{\text{ext}}}{L_z} = \frac{(en_z)^2}{\varepsilon_0} \frac{\omega_{\pm} e^{-2\frac{\omega_{\pm} y_0}{v}}}{[1 + \partial_{\omega}(\varepsilon_r \omega) - \partial_{\omega}(\varepsilon_g \omega) \text{sgn}(v)]_{\omega=\omega_{\pm}}}. \quad (\text{C4})$$

In particular, the stopping power may be written as in Eq. (16) of the main text.

#### 2. Pointlike beam

For a pointlike beam, we have  $\mathbf{j}_0(y, z) = -ev\delta(z) \delta(y - y_0) \hat{\mathbf{u}}_1$ . Therefore, by applying the quasistatic approximation to Eq. (B10), it is found that

$$P_{\text{ext}} = \frac{(ev)^2}{4\pi} \int d^2\mathbf{k} \delta(\omega_{\mathbf{k}} - k_x v) |\mathbf{E}_{\mathbf{k}}(y_0) \cdot \hat{\mathbf{x}}|^2. \quad (\text{C5})$$

Using  $\mathbf{E}_{\mathbf{k}} \approx -\nabla\phi_{\mathbf{k}}$  and Eq. (14) it follows that

$$\begin{aligned} P_{\text{ext}} &= \frac{e^2 v^2}{4\pi} \int d^2\mathbf{k} \delta(\omega_{\varphi} - k_x v) k_x^2 |A_{\mathbf{k}}|^2 e^{-2k_{\parallel} y_0} \\ &= \frac{e^2 v^2}{4\pi \varepsilon_0} \int_{v \cos \varphi > 0} d\varphi \frac{1}{|v \cos \varphi|} \\ &\quad \times (k_{\parallel} \cos \varphi)^2 a_{\varphi} e^{-2k_{\parallel} y_0} \Big|_{k_{\parallel} = \frac{\omega_{\varphi}}{v \cos \varphi}}. \end{aligned} \quad (\text{C6})$$

In the second identity, we switched to polar coordinates  $[(k_x, k_z) = k_{\parallel}(\cos \varphi, \sin \varphi)]$  and introduced  $a_{\varphi} = \varepsilon_0 k_{\parallel} |A_{\mathbf{k}}|^2$ , which only depends on the angle of the transverse wave vector, not on the amplitude. From the above result, one readily obtains Eq. (17) of the main text.

- 
- [1] F. D. M. Haldane and S. Raghu, Possible Realization of Directional Optical Waveguides in Photonic Crystals with Broken Time-Reversal Symmetry, *Phys. Rev. Lett.* **100**, 013904 (2008).
- [2] S. Raghu and F. D. M. Haldane, Analogs of quantum-Hall-effect edge states in photonic crystals, *Phys. Rev. A* **78**, 033834 (2008).
- [3] L. Lu, J. D. Joannopoulos, and M. Soljacic, Topological photonics, *Nat. Photon.* **8**, 821 (2014).
- [4] T. Ozawa, H. M. Price, A. Amo, N. Goldman, M. Hafezi, L. Lu, M. C. Rechtsman, D. Schuster, J. Simon, O. Zilberberg, and I. Carusotto, Topological photonics, [arXiv:1802.04173](https://arxiv.org/abs/1802.04173).
- [5] Z. Wang, Y. Chong, J. D. Joannopoulos, and M. Soljacic, Observation of unidirectional backscattering immune topological electromagnetic states, *Nature (London)* **461**, 772 (2009).
- [6] M. G. Silveirinha, Chern invariants for continuous media, *Phys. Rev. B* **92**, 125153 (2015).
- [7] M. G. Silveirinha, Bulk-edge correspondence for topological photonic continua, *Phys. Rev. B* **94**, 205105 (2016).
- [8] M. G. Silveirinha, Topological angular momentum and radiative heat transport in closed orbits, *Phys. Rev. B* **95**, 115103 (2017).
- [9] A. B. Khanikaev, S. H. Mousavi, W.-K. Tse, M. Kargarian, A. H. MacDonald, and G. Shvets, Photonic topological insulators, *Nat. Mater.* **12**, 233 (2013).
- [10] X. Cheng, C. Jouvaud, X. Ni, S. H. Mousavi, A. Z. Genack and A. B. Khanikaev, Robust reconfigurable electromagnetic pathways within a photonic topological insulator, *Nat. Mater.* **15**, 542 (2016).
- [11] M. C. Rechtsman, J. M. Zeuner, Y. Plotnik, Y. Lumer, D. Podolsky, F. Dreisow, S. Nolte, M. Segev, and A. Szameit, Photonic Floquet topological insulators, *Nature (London)* **496**, 196 (2013).
- [12] W. Gao, M. Lawrence, B. Yang, F. Liu, F. Fang, B. Béri, J. Li, and S. Zhang, Topological Photonic Phase in Chiral Hyperbolic Metamaterials, *Phys. Rev. Lett.* **114**, 037402 (2015).
- [13] M. G. Silveirinha, Quantized angular momentum in topological optical systems, [arXiv:1803.07121](https://arxiv.org/abs/1803.07121).

- [14] N. P. Armitage, E. J. Mele, and A. Vishwanath, Weyl and Dirac semimetals in three-dimensional solids, *Rev. Mod. Phys.* **90**, 015001 (2018).
- [15] X. Wan, A. M. Turner, A. Vishwanath, and S. Y. Savrasov, Topological semimetal and Fermi-arc surface states in the electronic structure of pyrochlore iridates, *Phys. Rev. B* **83**, 205101 (2011).
- [16] A. B. Sushkov, J. B. Hofmann, G. S. Jenkins, J. Ishikawa, S. Nakatsuji, S. Das Sarma, and H. D. Drew, Optical evidence for a Weyl semimetal state in pyrochlore  $\text{Eu}_2\text{Ir}_2\text{O}_7$ , *Phys. Rev. B* **92**, 241108(R) (2015).
- [17] J. Hofmann and S. D. Sarma, Surface plasmon polaritons in topological Weyl semimetals, *Phys. Rev. B* **93**, 241402 (2016).
- [18] P. A. Cherenkov, Visible emission of clean liquids by action of  $\gamma$  radiation, *Dokl. Akad. Nauk SSSR* **2**, 451 (1934).
- [19] S. J. Smith and E. M. Purcell, Visible light from localized surface charges moving across a grating, *Phys. Rev.* **92**, 1069 (1953).
- [20] L. D. Landau, E. M. Lifshitz, and L. P. Pitaevskii, *Electrodynamics of Continuous Media* (Butterworth-Heinemann, Oxford, 1985).
- [21] V. G. Veselago, The electrodynamics of substances with simultaneously negative values of  $\epsilon$  and  $\mu$ , *Sov. Phys. Usp.* **10**, 509 (1968).
- [22] C. Luo, M. Ibanescu, S. G. Johnson, and J. D. Joannopoulos, Cherenkov radiation in photonic crystals, *Science* **299**, 368 (2003).
- [23] X. Lin, S. Easo, Y. Shen, H. Chen, B. Zhang, J. D. Joannopoulos, M. Soljacic, and I. Kaminer, Controlling Cherenkov angles with resonance transition radiation, *Nat. Phys.* **14**, 816 (2018).
- [24] M. G. Silveirinha, Optical Instabilities and Spontaneous Light Emission by Polarizable Moving Matter, *Phys. Rev. X* **4**, 031013 (2014).
- [25] J.-K. So, J.-H. Won, M. A. Sattorov, S.-H. Bak, K.-H. Jang, G.-S. Park, D. S. Kim, and F. J. Garcia-Vidal, Cherenkov radiation in metallic metamaterials, *Appl. Phys. Lett.* **97**, 151107 (2010).
- [26] D. E. Fernandes, S. I. Maslovski, and M. G. Silveirinha, Cherenkov emission in a nanowire material, *Phys. Rev. B* **85**, 155107 (2012).
- [27] T. A. Morgado, D. E. Fernandes, and M. G. Silveirinha, Analytical solution for the stopping power of the Cherenkov radiation in a uniaxial nanowire material, *Photonics* **2**, 702 (2015).
- [28] V. V. Vorobev and A. V. Tyukhtin, Nondivergent Cherenkov Radiation in a Wire Metamaterial, *Phys. Rev. Lett.* **108**, 184801 (2012).
- [29] F. Liu, L. Xiao, Y. Ye, M. Wang, K. Cui, X. Feng, W. Zhang, and Y. Huang, On-chip integrated cherenkov radiation emitter eliminating the electron velocity threshold, *Nat. Photonics* **11**, 289 (2017).
- [30] M. G. Silveirinha, Low energy Cherenkov glow, *Nat. Photonics* **11**, 269 (2017).
- [31] X. Shi, X. Lin, F. Gao, H. Xu, Z. Yang, and B. Zhang, Caustic graphene plasmons with Kelvin angle, *Phys. Rev. B* **92**, 081404 (2015).
- [32] I. Kaminer, Y. Katan, H. Buljan, Y. Shen, O. Ilic, J. López, L. Wong, J. D. Joannopoulos, and M. Soljacic, Efficient plasmonic emission by the quantum Cherenkov effect from hot carriers in graphene, *Nat. Commun.* **7**, 11880 (2016).
- [33] X. Shi, X. Lin, I. Kaminer, F. Gao, Z. Yang, J. D. Joannopoulos, M. Soljacic, and B. Zhang, Superlight inverse Doppler effect, *Nat. Phys.* (2018).
- [34] T. M. Shaffer, E. C. Pratt, and J. Grimm, Utilizing the power of Cherenkov light with nanotechnology, *Nat. Nanotech.* **12**, 106 (2017).
- [35] E. D. Palik, R. Kaplan, R. W. Gammon, H. Kaplan, R. F. Wallis, and J. J. Quinn II, Coupled surface magnetoplasmon-optic-phonon polariton modes on InSb, *Phys. Rev. B* **13**, 2497 (1976).
- [36] J. A. Bittencourt, *Fundamentals of Plasma Physics*, 3rd ed. (Springer-Verlag, New York, 2010).
- [37] R. E. Camley, Nonreciprocal surface waves, *Surf. Sci. Rep.* **7**, 103 (1987).
- [38] A. R. Davoyan and N. Engheta, Theory of Wave Propagation in Magnetized Near-Zero-Epsilon Metamaterials: Evidence for One-Way Photonic States and Magnetically Switched Transparency and Opacity, *Phys. Rev. Lett.* **111**, 257401 (2013).
- [39] A. Davoyan and N. Engheta, Electrically controlled one-way photon flow in plasmonic nanostructures, *Nat. Commun.* **5**, 5250 (2014).
- [40] M. G. Silveirinha, S. A. H. Gangaraj, G. W. Hanson, and M. Antezza, Fluctuation-induced forces on an atom near a photonic topological material, *Phys. Rev. A* **97**, 022509 (2018); S. A. H. Gangaraj, G. W. Hanson, M. Antezza, and M. G. Silveirinha, Spontaneous lateral atomic recoil force close to a photonic topological material, *Phys. Rev. B* **97**, 201108(R) (2018).
- [41] D. N. Astrov, Magnetolectric effect in chromium oxide, *J. Expt. Theor. Phys. (U.S.S.R.)* **40**, 1035 (1961) [*Sov. Phys. JETP* **13**, 729 (1961)].
- [42] S. Coh and D. Vanderbilt, Canonical magnetic insulators with isotropic magnetoelectric coupling, *Phys. Rev. B* **88**, 121106 (2013).
- [43] R. S. K. Mong, A. M. Essin, and J. E. Moore, Antiferromagnetic topological insulators, *Phys. Rev. B* **81**, 245209 (2010).
- [44] V. Dziom, A. Shuvaev, A. Pimenov, G. V. Astakhov, C. Ames, K. Bendias, J. Böttcher, G. Tkachov, E. M. Hankiewicz, C. Brüne, H. Buhmann, and L. W. Molenkamp, Observation of the universal magnetoelectric effect in a 3D topological insulator, *Nat. Commun.* **8**, 15197 (2017).
- [45] F. R. Prudêncio, S. A. Matos, and C. R. Paiva, Asymmetric band diagrams in photonic crystals with a spontaneous nonreciprocal response, *Phys. Rev. A* **91**, 063821 (2015).
- [46] F. R. Prudêncio and M. G. Silveirinha, Optical isolation of circularly polarized light with a spontaneous magnetoelectric effect, *Phys. Rev. A* **93**, 043846 (2016).
- [47] R. L. Mather, Čerenkov radiation from protons and the measurement of proton velocity and kinetic energy, *Phys. Rev.* **84**, 181 (1951).
- [48] M. G. Silveirinha, Topological Classification of Chern-type insulators by means of the Photonic Green Function, *Phys. Rev. B* **97**, 115146 (2018).
- [49] M. G. Silveirinha, Modal expansions in dispersive material systems with application to quantum optics and topological photonics, [arXiv:1712.04272](https://arxiv.org/abs/1712.04272).